

# Bubble Chamber

D. Neto et al.<sup>1</sup>

<sup>1</sup>*Department of Physics, University of Illinois at Chicago, Chicago xxx, USA*

(Dated: December 16, 2019)

PACS numbers:

## I. INTRODUCTION

Radiative capture nuclear reactions are of fundamental importance in astrophysics. Protons, neutrons and helium are abundant in many stellar environments and can interact with heavier nuclei under hydrostatic and explosive conditions or in the Big Bang. Among these three particles, reactions that involve  $\alpha$  particles usually have the lowest cross sections as the higher Coulomb barrier between the nuclei reduces the penetrability of the capture processes. In most cases the cross sections are so small that it is impossible to measure these reactions at stellar energies in the laboratory using current technologies. One possible method for improving the quality of these measurements is to take advantage of the time-reversal symmetry of nuclear reactions that involve the strong and the electromagnetic interactions and measure the photodisintegration of nuclei into a light ion (proton, neutron, or  $\alpha$  particle) and a heavier residual nucleus. Because of phase space transformations, photodisintegration reactions can have cross sections which are orders of magnitude higher than the corresponding radiative capture process. Since the underlying matrix elements are identical for both processes, the cross sections can be measured by both, radiative capture or photo dissociation.

Traditional experiments (Ref.) measure the radiative capture cross sections in direct kinematics (i.e. a light ion beam on a heavy target) or in inverse kinematics (a heavy ion beam on a light target) usually detecting the  $\gamma$  ray in the exit channel. More recent techniques detect the recoiling heavy ion (Ref.) and in more complex experimental setups both the  $\gamma$  ray and the recoil in coincidence (Ref.). Ubiquitous beam and target contaminations and contributions from cosmic rays are usually the main sources of background that limit the sensitivity of the experiments. Furthermore the low density of the targets used in the experiments ( $\sim 1\text{-}10\text{ }\mu\text{g}/\text{cm}^2$ ) prolongs the time needed to measure the cross sections, thus increasing the contributions from cosmic rays and other environmental backgrounds as well.

The method described in this paper uses a thick ( $\sim 1\text{-}10\text{ g}/\text{cm}^2$ ) liquid target and a  $\gamma$  ray beam and can be adapted for measuring some of the most important nuclear reactions in stellar environments. The luminosity of this technique can therefore be orders of magnitude higher than that of some of the best direct measurements

performed to date using existing  $\gamma$ -ray facilities (ref.).

In the experiments discussed in this article the residual particles from the photodisintegration are detected with a bubble chamber. The prime example of a radiative capture process that can be studied with this photodissociation technique is the  $^{12}\text{C}(\alpha, \gamma)^{16}\text{O}$  reaction using an oxygen containing liquid such as  $\text{N}_2\text{O}$ . While this reaction is key for understanding the nucleosynthesis in the universe, it has the handicap that oxygen is not a monoisotopic element and, thus, requires the use of highly enriched  $^{16}\text{O}$  compounds.

In a first series of experiments we have therefore studied the photodisintegration reaction  $^{19}\text{F}(\gamma, \alpha)^{15}\text{N}$ . The inverse  $^{15}\text{N}(\alpha, \gamma)^{19}\text{F}$  reaction is the last step in the reaction chain leading to the nucleosynthesis of fluorine in Asymptotic Giant Branch or Wolf-Rayet stars (Ref.). Since  $^{19}\text{F}$  is a monoisotopic element no background reactions from the photodisintegration of other fluorine isotopes can occur. Furthermore through the use of fluorine containing compounds (e.g.  $\text{CH}_2\text{FCF}_3$  or  $\text{C}_4\text{F}_{10}$ ) in Dark Matter experiments (Ref.) sufficient information on the use of these liquids in bubble chambers is available in the literature. Since in the  $^{15}\text{N}(\alpha, \gamma)^{19}\text{F}$  reaction excited states in  $^{19}\text{F}$  are populated as well, no direct comparison between the radiative capture and photodissociation yields can be made. However, sufficient information about energies, widths and branching ratios of the critical states in  $^{19}\text{F}$  is available to calculate the expected yields for the  $^{19}\text{F}(\gamma, \alpha)^{15}\text{N}$  reaction.

An additional advantage of a bubble chamber for  $(\gamma, \alpha)$  measurements is the insensitivity of a bubble chamber to the incoming  $\gamma$ -beam. Measurements with high intensity  $\gamma$  sources have obtained sensitivity values below  $10^{-12}$  limited by the strength of the radioactive sources used in the experiments (Ref FNAL).

The first  $(\gamma, \alpha)$  experiments were performed using a tunable  $\gamma$ -ray beam from the HI $\gamma$ S facility at Duke University (Ref.) from inverse Compton scattering of laser light produced by electrons circulating in a storage ring (Ref. PLB and NIMA). In these first experiments an excellent agreement between direct  $(\alpha, \gamma)$  measurements and the time-inverse  $(\gamma, \alpha)$  experiments was observed (Ref. PLB) covering the  $(\alpha, \gamma)$  cross section range from  $10\text{ }\mu\text{b}$  to about  $3\text{ nb}$ , limited by background reactions between electrons and the residual gas in the storage ring (Ref. NIMA).

In this paper we describe an extension of these mea-

surements towards lower energies and cross sections using a Bremsstrahlung beam from the electron injector at Jefferson Lab.

## II. EXPERIMENTAL DETAILS

### (a) The Single Fluid Bubble Chamber

Bubble chambers, invented more than 60 years ago [Glaser book] as experimental tools in high-energy physics have in the last decade found a new application as continuously operating superheated detectors for the search of Dark Matter [DM1,DM2,DM3,DM4]. While the original bubble chambers for high-energy experiments (sometimes called "dirty chambers") were in a superheated state for only a short period of time ( $\sim$ msecs), coincident with the arrival of the beam pulse from the accelerator, the dark matter chambers have to be active for extended time periods (minutes-hours), which was achieved by replacing the "piston" used for changing the pressure in the detector with a so-called buffer fluid. In the literature these detectors are called "clean chambers" [xx]. Bubble chambers used as active targets for nuclear astrophysics experiments are employing the same technique [Ugalde]. The main difficulty with this technique originates from chemical reactions and the solubility between the active target and the buffer fluids. While this was not a problem for the  $^{19}\text{F}(\gamma, \alpha)^{15}\text{N}$  reaction, the first system studied with this technique, which used superheated  $\text{C}_4\text{F}_{10}$  and  $\text{H}_2\text{O}$  as a buffer fluid [Ugalde], later experiments with superheated  $\text{H}_2\text{O}$ ,  $\text{CO}_2$  and  $\text{N}_2\text{O}$  fluids and utilizing fluorinated oils, water or Hg as buffer fluids lead to the formation of hydro-fluoric acid, clathrates, oxides, nitrides, and dissolved buffer fluids in the fiducial volume which prevented their use as active detector systems [Digiovine0]. These chemical reactions can be avoided by using a so-called 'single fluid bubble chamber'.

Single fluid ("clean") bubble chambers have first been used for the detection of long-lived, low-activity radioisotopes ( $^{14}\text{C}$ , U or T) dissolved in diethyl ether or propane [Dodd, Brautti, Waters]. The single-fluid bubble chamber in this experiment is based on the detector used in our earlier experiment [Ugalde] and described in more detail in Ref. [Digiovine].

The operational principle of a single-fluid bubble chamber is explained in Fig. 1, which shows the phase diagram of  $\text{C}_3\text{F}_8$ . At a temperature of  $18^\circ\text{C}$  and a pressure of 2 MPa the  $\text{C}_3\text{F}_8$  is in its liquid phase. Lowering the pressure to 0.5 MPa (red line in Fig. 1) brings the liquid into a superheated state which, since the products of a photodisintegration reaction deposits  $\sim 1$  MeV in the liquid, leads to the formation of a bubble. The same procedure performed at a temperature of  $-5^\circ\text{C}$  (blue line in Fig. 1) does not cross the liquid-vapor barrier and, thus, will not

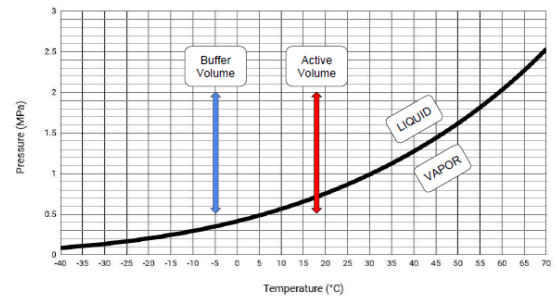


FIG. 1: Phase diagram (pressure vs temperature) of  $\text{C}_3\text{F}_8$ . The red line shows the region covered in the fiducial region bombarded by the Bremsstrahlung beam. This line crosses the phase boundary and creates a superheated liquid which can lead to bubble formation. The blue line at lower temperature does not cross the phase boundary and, thus, does not lead to bubble formation.

result in bubble formation.

A schematic of the single-fluid chamber used in our experiment is shown in Fig. 2. A cylindrical glass vessel (diameter 3.6 cm) filled with  $\text{C}_3\text{F}_8$  is located in a box-shaped high-pressure container. The glass vessel is surrounded by xx cm of oil and the temperature inside the main part of the high-pressure volume is kept at  $18^\circ\text{C}$ . The pressure in the high-pressure vessel can be changed from 0.5 MPa to 2 MPa. The  $\text{C}_3\text{F}_8$  filled glass vessel is bombarded by a collimated bremsstrahlung beam of 4-5 MeV gammas from the injector of the electron accelerator at Jefferson Lab. Details of the beam production are presented in Section II.b. The glass vessel is continuously scanned by a 100 Hz high-sensitivity CMOS camera mounted in a container shielded by xx cm of Pb which is located outside of the pressure vessel. If  $\gamma$ 's from the bremsstrahlung beam interact with the fluorine via the  $^{19}\text{F}(\gamma, \alpha)^{15}\text{N}$  reaction, the  $^{15}\text{N}$  and alpha particles in the outgoing channel are stopped in the superheated  $\text{C}_3\text{F}_8$  liquid ( $p=0.5$  MPa) which leads to the formation of a small bubble in the superheated  $\text{C}_3\text{F}_8$ . If a bubble is observed by the camera, 10 consecutive frames taken at 10 ms intervals are stored in the computer providing information about the location and the movement of the bubble in the fluid. At the same time the pressure in the bubble chamber is increased to 2 MPa which is above the critical pressure for  $\text{C}_3\text{F}_8$  leading to a quenching of the bubble. After a recovery time of 5-10 sec the pressure is again decreased to the superheated region below 0.58 MPa. In the first experiment at the HI $\gamma$ S facility the superheated fluid was scanned by two cameras through windows located at  $45^\circ$  and  $135^\circ$  with respect to the beam. This allowed us to generate a 3D picture

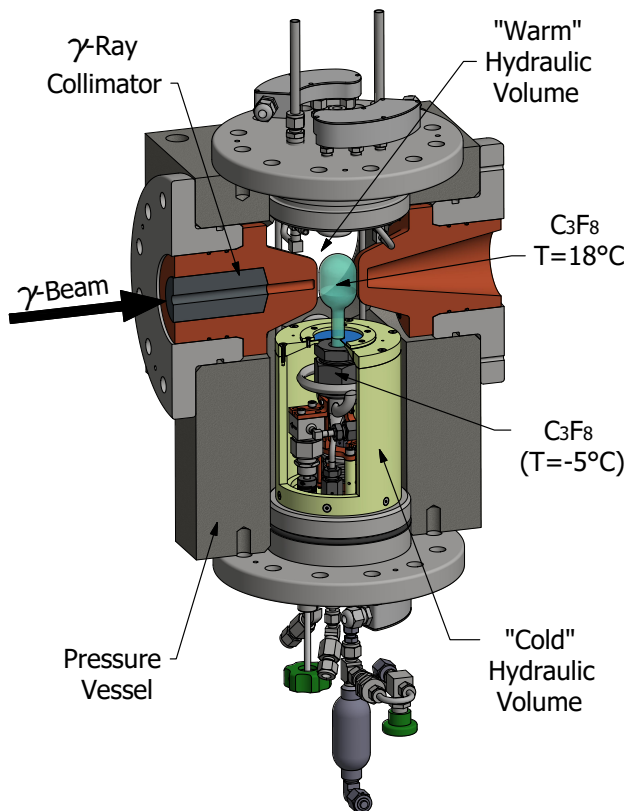


FIG. 2: Schematic of the bubble chamber used in the experiment. See text for details.

of the bubble for the elimination of background events produced in the walls of the glass vessel [?]. Space limitations in the pressure vessel and the need to shield the CMOS camera from the bremsstrahlung background at JLAB prevented the use of two cameras. Details will be discussed in Section III.

Information about the thermodynamics of bubble formation and the pressure control system used in the experiment can be found in Ref. [Digiovine]. The main difference between the single-fluid bubble chamber used in this experiment and the one described in Ref. [Digiovine] is the absence of a buffer fluid. In order to avoid bubble formation in the  $C_3F_8$  outside the area scanned by the CMS camera the whole region below the glass vessel containing the superheated  $C_3F_8$  is surrounded by a separate cylindrical container and kept at lower temperatures (see Fig. 2). The required temperature can be obtained from the p-T curve for  $C_3F_8$  in Fig. 1. Operating the bubble chamber at a temperature of  $18^\circ C$  in the pressure range from 0.58 MPa (superheated) to 2 MPa (not superheated) requires lowering the temperature by about  $20\text{--}25^\circ C$  in the area where bubble generation is to be prevented. As shown in Fig. 2 a cold region is created using a cooling circuit inside a cylindrical thermal break

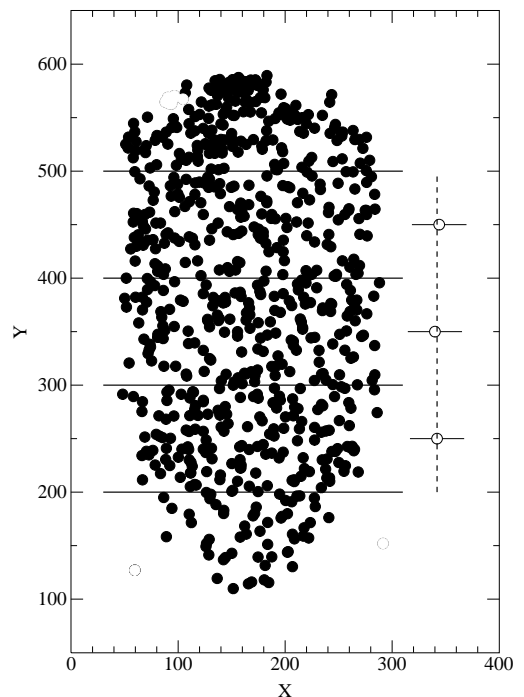


FIG. 3: Events observed in the single-fluid bubble chamber with a  $Pu^{13}C$  neutron source. The count rates and the associated statistical uncertainties in three adjacent vertical sections of the bubble chamber are shown in the right side of the figure.

(shown in yellow in Fig. 2) which is kept below  $-5^\circ C$ . Thus, the temperature of the  $C_3F_8$  in the lower part of the glass vessel, in the bellows and the plumbing system never crosses the liquid-vapor phase boundary shown in Fig. 1, allowing the same fluid being used as active target and buffer fluid. The temperature distribution was measured with 14 RTDs mounted outside the glass vessel and verified in several long-term measurements using a  $Pu^{13}C$  neutron source, located at distances between 1 m and 7 m from the detector. The distribution of the bubbles measured in the glass vessel is shown in Fig. 3. The number of bubbles detected in the cylindrical part of the vessel with this neutron source is shown by the solid squares on the right side of Fig. 3. It is found to be constant within the main volume of the glass vessel.

### (b) Production of the Bremsstrahlung beam, energy, current and beam measurements

The electron beam at Jefferson Lab's injector was produced from a photo-cathode source operating at 130 kV with GaAs [?] as photo-cathode material. After bunching at 130 keV, the beam was accelerated to 500 keV with a 5-cell low Q graded  $\beta$  radiofrequency (RF) cavity before being accelerated to 5-6 MeV in two 5-cell superconducting RF cavities known as the 'quarter cryomodule'. After the quarter cryomodule the electron beam is transported to a dipole magnet which is followed by four beamlines. The straight section (0L) delivers the beam to the next stage of acceleration before it merges into the main CE-BAF accelerator, while the three other beam lines (2D, 3D, and 5D) serve experimental stations mounted at  $-30^\circ$ ,  $xx^\circ$  and  $+25^\circ$ , respectively. The bubble chamber was installed at the 5D ( $+25^\circ$  line). Setting and measuring the electron beam characteristics for the experiment used the equipment installed in 0L, 5D, and 2D lines. The  $\gamma$ -bremsstrahlung beam was produced in a water-cooled 5 mm thick Cu radiator consisting of high-purity oxygen-free copper mounted xx cm in front of the bubble chamber. A Cu collimator then reduced the dimension of the incident  $\gamma$  beam to a diameter of 10 mm at the bubble chamber.

Throughout the experiment, the cavities in the 'quarter cryomodule' were operated 'on-crest', i.e. providing maximum energy gain from each cavity. The gradient setpoints of the two cavities were adjusted to set the momentum of the beam to match the calculated spectrometer dipole setting for the desired beam momentum in the 5D line where the bubble chamber was mounted. Beam position monitors (BPM) in the 2D and 5D line determined when the momentum matched the required dipole setting. The momentum was measured under the assumptions that the momentum of the beam coming into the spectrometer dipole is fixed and proportional to the angle (and therefore the dipole setting) required to bend the beam into the respective beam line. Wire scanners in the 2D and 5D beamlines were used to extrapolate the size of the beam spot on the Cu radiator which are typically between 0.3 and 1.5 mm. The beam momenta measured with this method are summarized in Fig.4. The associated errors are typically 0.18% dominated by uncertainties in the ion-optical transport calculations of the computer program [?]. The rms-beamspot size at the radiator was measured to be between 0.3 and 1.6 mm with currents ranging from 50 nA to 50  $\mu$ A as measured by a xxxxx.

## III. EXPERIMENTAL RESULTS

With the experimental setup described in the previous section an excitation function for the photodissociation

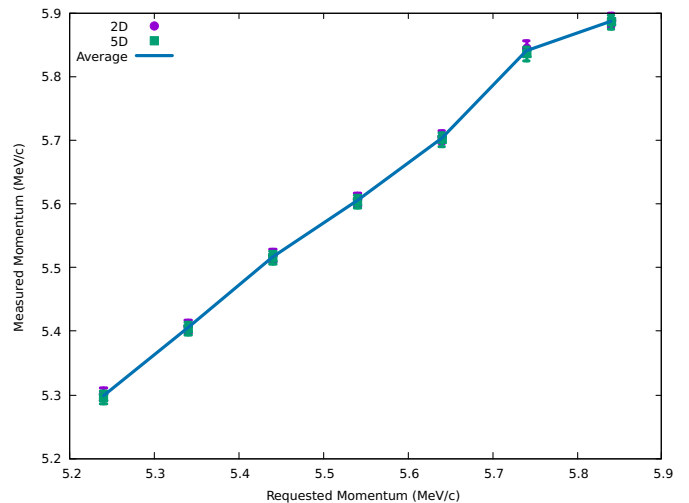


FIG. 4: Beam momenta measured in the 2D and 5D beam lines and the associated uncertainties vs. the design momenta covering the kinetic energy range of 4.809 - 5.397 MeV

reaction  $^{19}\text{F}(\gamma, \alpha)^{15}\text{N}$  was measured in the energy range from 4 MeV-5.39 MeV. The location of the bubbles in the 10 consecutive pictures mentioned in Section II were analyzed with a software package which allowed to select bubbles with similar radii and velocities. Details of this analysis will be published in a separate paper([?]).

### a) Sources of background events

In addition to the bubbles generated by the  $^{19}\text{F}(\gamma, \alpha)^{15}\text{N}$  reaction in the superheated  $\text{C}_3\text{F}_8$  fluid there are several sources of background events in this experiment. One originates from the decay of radioactive elements (Th, U) present in minute amounts in the material used for the construction of the detector and the second from cosmic rays that are detected in the bubble chamber. In addition to these two sources which do not depend on the intensity of the incoming Bremsstrahlung beam there are other background events which originate from two-step processes consisting of a  $(\gamma, n)$  reaction on deuterium or  $^{17}\text{O}$  present e.g. in the oil surrounding the bubble chamber or in the walls of the glass vessel, followed by elastic n-scattering in the superheated  $\text{C}_3\text{F}_8$  liquid or  $(n, \alpha)$  reactions in the glass.

Since bubble chambers are insensitive to  $\gamma$ -radiation there is no problem with background from  $\gamma$  emitting isotopes such as  $^{40}\text{K}$ . To eliminate the contributions from  $\alpha$ -emitting isotopes (e.g.  $^{226}\text{Ra}$ ) the same cleaning procedures as prescribed for the Dark Matter experiments have been employed (Ref. (PICO)) where typical event rates from  $\alpha$ 's in the walls of the glass vessel are xx events/cm<sup>2</sup>/sec.

The main contribution from cosmic rays originates

from (secondary) neutrons which, at sea level, have a flux of  $\sim 0.01$  neutrons/cm<sup>2</sup>/sec. Myons, which, after neutrons, are the second most abundant particles in the cosmic-ray flux do not lead to bubble formation under the operating conditions of the bubble chamber used in this experiment. During the experiment the cosmic background rate has been measured over a period of xx days and was found to be about  $5 \times 10^{-2}$  events/sec, in good agreement with the expected flux from cosmic ray neutrons.

The main source of beam-induced background originates from neutrons produced by the bremsstrahlung beam in any material where the neutron separation energy is below the electron beam energy. These neutrons can then elastically scatter from the superheated fluid and the nuclear recoils will produce a bubble if their recoil energy is high enough. For the beam energies and the materials used in this experiment, only photodisintegration from deuterium with the low binding energy of 2.2 MeV or <sup>17</sup>O (4.14 MeV) can produce sufficiently energetic neutrons. These isotopes are present in the surrounding hydraulic fluid (mineral oil) and in the walls of the glass vessel.

### b) Distribution of bubbles

The location of bubble events taken at four energies are shown in Fig. 5. Each spectrum was accumulated over a period of about 1 hour (??) with currents that vary by three orders of magnitude (from 54 nA at 5.35 MeV to 48  $\mu$ A at 4.00 MeV). At the highest energies the data overlap with the previous experiment performed at the HI $\gamma$ S facility while the energy of 4.00 MeV is below the <sup>19</sup>F( $\gamma$ ,  $\alpha$ )<sup>15</sup> threshold located at 4.014 MeV. Since the bremsstrahlung beam passes through a xx cm long, 1 cm diameter Cu collimator, photodissociation events in the C<sub>3</sub>F<sub>8</sub> fluid have to be located in a cylinder-shaped fiducial area whose projection is shown by the solid red lines in Fig. 5. Events outside of the fiducial area are caused by background events in the wall of the glass vessel (e.g. from the <sup>10</sup>B(n,  $\alpha$ )<sup>7</sup>Li reaction) ([? ]) which, because of the short range of charged particles, are concentrated in the vicinity of the glass surface (Ref.[? ]). In order to subtract events from cosmic rays and two-step processes, mentioned above, a background area was defined below the fiducial area as shown by the black lines in Fig. 5. At the highest energy (5.35 MeV), corresponding to a cross section of 6  $\mu$ b the contribution of the two-step processes is quite small. Increasing the incident electron beam, however, leads to an increased neutron flux from d( $\gamma$ , n)p reactions in the oil surrounding the glass vessel and the production of charged particles via the <sup>10</sup>B(n,  $\alpha$ )<sup>7</sup>Li reaction in the boron material in the inner side of the glass vessel. These events, again concentrated by refraction effects clearly mark the shape of the bubble chamber and set a limit to the cross sections that can be measured.

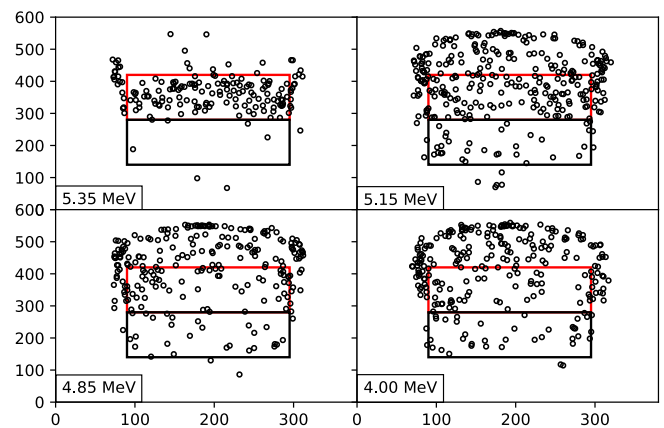


FIG. 5: Distribution of events measured in the bubble chamber at various bombarding energies using a bremsstrahlung beam with energies of  $E_\gamma$ . The electron currents as well as the calculated cross sections of the <sup>15</sup>N( $\alpha$ ,  $\gamma$ )<sup>19</sup>F at these energies are included. (see text for details).

Possible improvements are discussed in the summary.

The cross sections calculated from the known resonance parameters and branching ratios of the <sup>15</sup>N( $\alpha$ ,  $\gamma$ )<sup>19</sup>F reaction [? ] cover the range from 6  $\mu$ b to  $\sim 40$  pb. These cross sections have then to be folded with the energy distribution of the bremsstrahlung beam which will be discussed in Section xx. The yields  $Y$  defined by  $(F-B)/I$ , where  $F$  and  $B$  are the (deadtime-corrected) rates observed in the fiducial and background areas, respectively and  $I$  is the incident electron current (in  $\mu$ A) are shown in Fig. xx. The range in yield covered in this experiment extends over more than four orders of

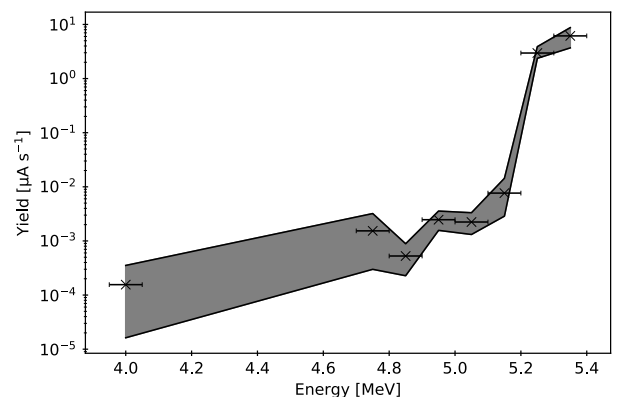


FIG. 6: Experimental yields defined by the equation  $(F-B)/I$  where  $F$  and  $B$  are the deadtime-corrected counts in the fiducial and background regions shown by the solid and dot-dashed lines in Fig. xx.  $I$  is the electron beam current (in  $\mu$ A) used for the production of the bremsstrahlung beam.

magnitude.

### Extraction of the cross section

The goal of this test experiment was the determination of cross section limits for  $(\alpha, \gamma)$  reactions that can be achieved by measuring the time-inverse photodissociation process and a study of the associated background reactions. Since for this application some of the parameters (e.g. the resonance energies) are known, two methods can be employed to extract the cross sections from the measured yields which are the results of a convolution between the energy-dependent reaction cross sections and the energy-dependent bremsstrahlung flux. This flux was determined using a Geant4 simulation from the beam parameters at each energy listed in Table ?? with an energy dependence fit to an FIXME 8th order Chebyshev polynomial.

The first method was to employ a one- or two-resonance model with a superimposed linear background. This involved performing a fit to the yield data assuming one or two three-parameter resonances convoluted with the photon flux superimposed on an incoherent background with a linear energy dependence to represent the neutron elastic or  $(n, \alpha)$  backgrounds. A Bayesian analysis was then performed with a likelihood function formed from the yield model to determine the 68% confidence intervals. The parameter phase space was explored using the Gibbs's sampling technique [?] with the collective absolute energy uncertainty treated as a nuisance parameter. The two resonances are shown in Fig. 7 and fits to the yields are shown in Fig. 8.

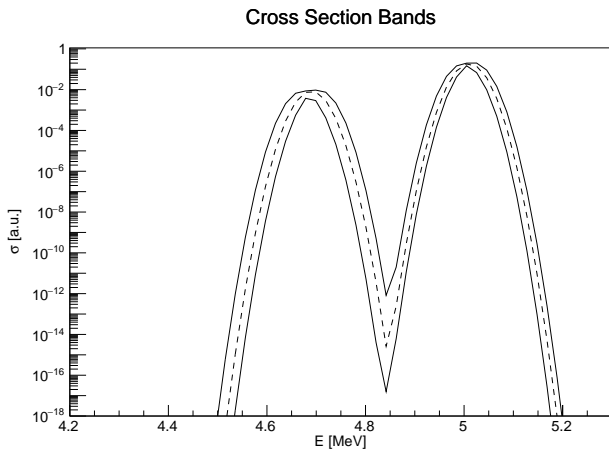


FIG. 7: This is not the final figure, since the two resonances are too close in strength. I stole the picture from Seamus' calculation. The deconvoluted cross sections using both the linear decomposition method (points with error bars) and 68% confidence interval bands under the single-resonance model (bands).

The second approach used the simple linear decomposition based on the Penfold-Leiss method [?]. Since the cross sections vary over several orders of magni-

tude, the energy bin-centers will be systematically biased towards higher energies in a way that depends on the cross section. An iterative method was developed using neighboring bins to determine the bias in a self-consistent method and makes few assumptions on the underlying structure. This iterative method was tested using pseudo-data using a single resonance and an additional systematic uncertainty on the centered energy of FIXME is assigned. The results are shown as points in Fig. 8.

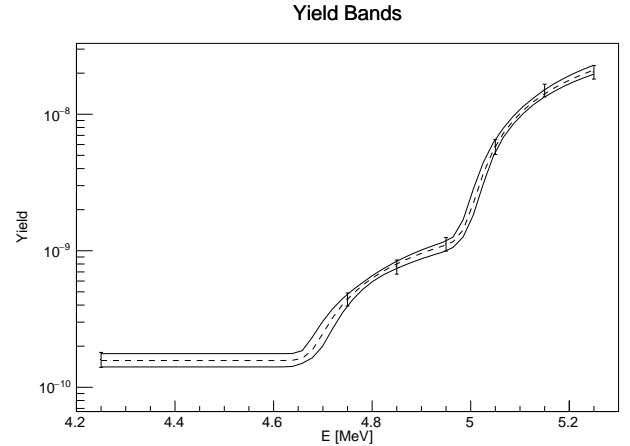


FIG. 8: The normalized random-background subtracted yields vs. electron beam energy and resulting 68% confidence interval bands under the single-resonance with superimposed linear background model.

Still to be written: Cross section limits obtained in this experiment.

### IV. FUTURE PLANS

While the experiment described in this paper produced cross section values for the  $^{15}\text{N}(\alpha, \gamma)^{19}\text{F}$  reaction in an energy region where so far only upper limits were available, further improvements to this technique are possible. (discussion of improvements of background suppression using two observation angles, additional neutron shielding, replacing the hydrogen in the oil to reduce gamma-ray induced neutrons,...) With these improvements cross section measurements of other important  $(\alpha, \gamma)$  reactions with cross sections in the pb range should become accessible. Some examples are given below.

With the exception of very low-mass stars, most stellar objects will pass through a period of helium burning. During this stage in the life of a star the size of the stellar core is determined. While the composition and density of the core vary throughout the life of a star, its mass is constant and determined by two competing processes: one that produces carbon via the triple  $\alpha$  particle reaction, and another that burns carbon to produce oxygen



with the  $^{12}\text{C}(\alpha, \gamma)^{16}\text{O}$  reaction (Ref.). As a consequence, the ratio of carbon to oxygen in the universe is defined by this thermonuclear process. Subsequent stages of stellar evolution in various scenarios will depend on the physics of the core –even if they do not occur in it. Whether a star at the end of its life cools down as a white dwarf or explodes as a supernova, leaving a neutron star or a black hole as a remnant is determined by the mass of the stellar core.

Helium burning via thermonuclear reactions is a process that depends strongly on the local temperature. The Coulomb repulsion between atomic nuclei lowers the cross section for the  $^{12}\text{C}(\alpha, \gamma)^{16}\text{O}$  reaction at temperatures between 0.15 GK and 0.35 GK to values of  $1 \times 10^{-17}$  b, which is many orders of magnitude below the limits of present experimental techniques ( $\sim 10^{-12}$  b) (Ref.). This reaction has been studied in normal and inverse kinematics and cross section limits in the  $\sim$ pb range have been obtained (Ref. RMP). For measurements of the photodissociation reaction  $^{16}\text{O}(\gamma, \alpha)^{12}\text{C}$  with a bubble chamber oxygen-containing superheated liquids of  $\text{H}_2\text{O}$ ,  $\text{CO}_2$  and  $\text{N}_2\text{O}$  have been tested so far (Ref. DiGiovine). The main difficulty for this reaction originates from the competing  $^{17}\text{O}(\gamma, \alpha)^{13}\text{C}$  and  $^{18}\text{O}(\gamma, \alpha)^{14}\text{C}$  reactions with Q-values of -6.357 MeV and -6.227 MeV, respectively, which are smaller than the one for photodissociation of  $^{16}\text{O}$  (Q=-7.162 MeV). Thus, this measurement requires the use of highly-enriched oxygen, in order to eliminate the contributions from the  $^{17,18}\text{O}$  isotopes.

Helium induced nuclear reactions are of importance in other astrophysical scenarios as well. The Big Bang produces primordial lithium with an abundance that shows a

discrepancy between observations and model predictions, which is known as the lithium problem (Ref.). While it is unlikely that the solution is of nuclear origin, one possibility involves the production of lithium through the  $^3\text{He}(^4\text{He}, \gamma)^7\text{Be}(\beta^+)^7\text{Li}$  process, but the radiative capture of  $\alpha$  particles on deuterium and tritium are two other possible nucleosynthetic paths to generate lithium. A bubble chamber containing a lithium compound dissolved in liquid ammonia is under consideration.

A bubble chamber with a liquid containing a magnesium solution could be used to study the photodisintegration of  $^{26}\text{Mg}$  to determine the rate of the  $^{22}\text{Ne}(\alpha, \gamma)^{26}\text{Mg}$  neutron poison reaction (Ref.). The weak component of the s process is responsible for the production of nuclei with  $60 \leq A \leq 90$  in massive stars. It requires a neutron density of  $\sim 1 \times 10^{12} \text{ cm}^{-3}$ , which is provided mainly by the  $^{22}\text{Ne}(\alpha, n)^{25}\text{Mg}$  reaction. The number of neutrons produced depends not only on the cross section but also on the rate of the  $^{22}\text{Ne}(\alpha, \gamma)^{26}\text{Mg}$  reaction –an alternate competing process that “poisons” the production of neutrons. Both rates are uncertain at temperatures relevant to the weak component of the s process.

## V. ACKNOWLEDGEMENTS

This work was supported by the US Department of Energy, Office of Nuclear Physics, under Contract No. DE-AC02-06CH11357 and